ACS Sustainable Chemistry & Engineering

pubs.acs.org/journal/ascecg

Research Article

Direct Laser Writing of Chitosan–Borax Composites: Toward Sustainable Electrochemical Sensors

Eoghan Vaughan,*,⊥ Chiara Santillo,⊥ Alessandra Imbrogno, Gennaro Gentile, Aidan J. Quinn, Saulius Kaciulis, Marino Lavorgna,* and Daniela Iacopino*

Cite This: ACS Sustainable Chem. Eng. 2023, 11, 13574–13583

Read Online

ACCESS | Metrics & More | Article Recommendations | Supporting Information

ABSTRACT: In this study, the laser-induced graphitization process of sustainable chitosan-based formulations was investigated. In particular, optimal lasing conditions were investigated alongside the effect of borax concentration in the chitosan matrix. In all cases, it was found that the obtained formulations were graphitizable with a CO_2 laser. This process gave rise to the formation of high surface area, porous, and electrically conductive laser-induced graphene (LIG) structures. It was found that borax, as a cross-linker of chitosan, enabled the graphitization process when its content was ≥30 wt % in the chitosan matrix, allowing the formation of an LIG phase with a significant content of graphite-like structures. The graphitization process was investigated by thermogravimetric analysis (TGA), Raman, X-ray photoemission (XPS), and Fourier transform infrared (FTIR) spectroscopies. LIG electrodes obtained from CS/40B formulations displayed a sheet resistance as low as 110 Ω/sq. Electrochemical characterization was performed after a 10 min electrode activation by cycling in 1 M KCl. A heterogeneous electron transfer rate, k^0, of 4×10^{-3} cm s^{-1} was determined, indicating rapid electron transfer rates at the electrode surface. These results show promise for the introduction of a new class of sustainable composites for LIG electrochemical sensing platforms.

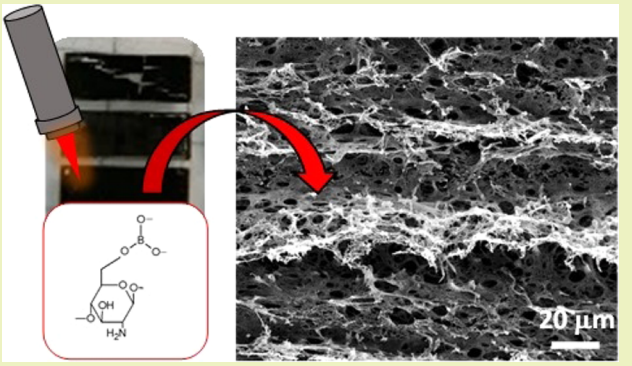

KEYWORDS: *laser-induced graphene, chitosan, composite, borax, char formation*

INTRODUCTION

Graphene is a material with renowned physical and electrical properties.[1] Graphene and graphene-like materials are used in areas, such as electronics, electrochemical sensing, strain sensors, energy storage, catalysis, and more.[2−6] The fabrication of graphene by standard methods, such as chemical vapor deposition, liquid-phase exfoliation, or micromechanical exfoliation, presents challenges relating to achieving a cost-effective and time-effective procedure suitable for commercialization.[7] Therefore, alternative fabrication methods, such as the use of a laser to reduce graphene oxide, creating graphene-like surface features, have been explored for more than a decade.[8−10] Recently, direct laser writing protocols have been developed and systematically applied for the conversion of commercial polymers to a high-quality graphene-like material.[11] Specifically, in 2014, Lin et al. obtained a graphene-like material, termed laser-induced graphene (LIG), by direct laser writing of a commercial Kapton tape (polyimide) with a CO_2 laser. LIG is a porous, three-dimensional (3D) structure, characterized by a high surface area, resulting from the generation of gases during the lasing process.[12] The LIG morphology, and hence its surface properties, can be tuned by controlling the laser parameters, such as power, speed, and laser wavelength.[13] LIG has been shown to be an excellent material for applications, such as electrochemical sensing, energy storage, humidity sensing, and biosensing, among others.[14−20]

Considering the extensive research currently being conducted into LIG-based devices and their wide range of applications, the sustainability of such materials must be considered.[21,22] In this scenario, it is worth considering alternatives to fossil fuel-derived polymers as precursor materials for LIG production. Although the detailed mechanism of laser-induced polymer graphitization is still not fully clear, it is known that LIG formation results from a combination of photothermal and photochemical processes, highly favored in Kapton by the aromatic structure of polyimide.[23] In recent years, various natural materials, such as wood, paper, leaves, coal, cloth, and cork, have been used as LIG precursor substrates alternative to polyimide,[15,24−28] and applications of the resulting "green" LIG structures have

Received: May 8, 2023
Revised: August 14, 2023
Published: September 1, 2023

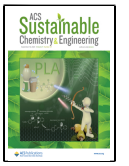

ranged from electrochemical sensors to supercapacitors. Natural materials are converted into LIG based on the same principles as polyimide conversion: adsorption of radiation, local increase of temperature, cleavage of C−C, C−O, and C−H bonds, and reorganization and polymerization of the aromatic structures into graphene-like structures.[29] Recently, attention has also been given to biopolymer materials, in an attempt to widen the range of graphitizable materials. For example, Larrigy et al. have successfully graphitized chitosan films using a multipass laser conversion technique based on a combination of CO_2 and 405 nm lasers.[30] The resulting LIG showed a porous morphology with low sheet resistance, below 40 Ω/sq, suitable for electrochemical sensing applications. Huang et al. converted eco-friendly chitosan-based derivatives into LIG with a one-step CO_2 laser engraving in ambient air.[31] Low sheet resistances of 12.7 Ω/sq were achieved with chitosan hydrochloride-based sheets; however, these films were too prone to deformation or cracking to be used as devices. Instead, carboxymethyl chitosan-based films, with sheet resistances of 2.2 kΩ/sq, showed suitability for eco-friendly electronics in the form of triboelectric nanogenerators. The introduction of chitosan into the range of natural LIG precursor materials is an important development due to its natural abundance, biocompatibility, biodegradability, non-toxicity, chemical stability, and high reactivity.[32] However, despite the above attractive properties, chitosan exhibits low chemical stability in wet environments, which limits its application fields.[32] Sodium tetraborate decahydrate (borax) has been recently investigated as a cross-linking agent to improve chitosan's mechanical and water barrier properties.[32,33] Specifically, it has been found that the esterification reaction between borate ions and the hydroxyl moieties of chitosan creates a composite structure denser than pristine chitosan, resulting in increased water and gas barrier properties.[34] Moreover, the incorporation of boron into cellulose-based materials (cotton, wood, and paper) has been shown to exhibit effective flame-retardant properties, leading to improved limiting oxygen index (LOI) values, reduced peak heat release rate (pHRR), and reduced smoke release.[34,35] In particular, when mixed to polymer matrices, borax provided a glass-like coating on the fire-exposed surface and promoted the formation of char, which is well known to consist of amorphous carbon as well as graphite-like structures, according to different high-temperature conditions.[36,37] Coelho et al. and separately Pinheiro et al. have shown that borax-treated chromatography paper can be converted into LIG structures, with electrochemical sensing and microsupercapacitor applications, respectively.[38,39] The role of borax is elucidated by a comparison with laser-treated raw chromatography paper. While the borax treatment allows the paper to withstand the photothermal degradation process, leading to LIG formation, the raw sample is completely ablated by the laser.

In this work, we introduced borax as a cross-linker of chitosan and investigated the graphitization properties of the resulting formulations by the use of infrared laser sources. Different concentrations of borax were used and it was found that a percentage ≥30% (wt, with respect to CS content) was effective in producing formulations graphitizable by one or two laser passes. The obtained LIG structures displayed high porosity, 3D morphology, and low sheet resistance. The potential use of this LIG material as an electrochemical sensor was investigated. It was found that LIG displayed a high heterogeneous electron transfer rate, comparable to the value found in other green LIG materials, indicating rapid electron transfer rates at the electrode surface. These results show promise for the introduction of a new class of sustainable formulations as LIG feedstock for the development of sustainable electrochemical sensing platforms.

EXPERIMENTAL SECTION

Materials. Medium-molecular-weight chitosan powder was purchased from Sigma-Aldrich. Gluconic acid δ-lactone (GDL) and sodium tetraborate decahydrate (borax) were supplied from Sigma-Aldrich (Italy). All solutions were prepared using deionized Milli-Q water (resistivity 18.2 MΩ.cm).

CS-Based Film Preparation. Chitosan (CS) powder was dissolved in a D-(+)-gluconic acid δ-lactone (GDL) aqueous solution at room temperature to prepare 20 mg mL^{-1} CS solution. Then, borax aqueous solution was added under stirring. The borax (B) concentration was varied to obtain a final content equal to 20, 30, 40, and 60 wt % with respect to the CS weight. Subsequently, the solution was poured into a glass plate and air-dried to allow solvent removal. The thickness of the obtained films was about 100 μm, measured by a micrometer screw gauge. CS-based films were coded CS/xB, where x represents the weight percentage of borax.

LIG Fabrication. LIG structures were fabricated by direct laser writing of CS/xB films with a CO_2 laser engraver (10.6 μm wavelength, 30 W power, HQ-3020B, GuangZhou Amonstar Trade Co., Ltd.). Laser power was varied between 8 and 15% (for higher powers, complete ablation of the material occurred). Laser speed was varied between 10 and 40%. In cases of combinations of low power and high speed, features were overlapped (written once, then again in the same spot, indicated by "×2" in the "Laser settings" column of Table S1) to investigate the effect of multiple laser passes. Conditions were sought, which produced an undamaged, black feature, indicating the formation of LIG.

Characterization. Surface morphology was analyzed using a Zeiss Supra scanning electron microscope (SEM) equipped with an Oxford X-Max 50 detector operating at an accelerating voltage of 10 kV. Bright-field transmission electron microscopy (TEM) analysis was performed by means of an FEI Tecnai G12 Spirit Twin (LaB6 source) at a 120 kV acceleration voltage. TEM images were collected on an FEI Eagle 4 k charge-coupled device (CCD) camera. Raman investigation was performed with a Renishaw inVia Raman system equipped with a 514 nm argon-ion laser. The focusing of the laser beam onto the sample was obtained through a Leica 20× objective with 0.4 N.A. Spectra were acquired at a laser power of 3 mW and an acquisition time of 10 s. Attenuated total reflection-Fourier transform infrared (ATR-FTIR) analysis was carried out with a portable Bruker α II's Platinum ATR single-reflection diamond ATR. X-ray photoemission (XPS) spectra were collected by using an Escalab 250Xi (Thermo Fisher Scientific, U.K.) spectrometer, equipped with a monochromatic Al Kα excitation source, electron and ion flood guns for charge neutralization and a 6-channeltron detection system. The photoemission spectra were collected at 20 eV pass energy, and the diameter of the analyzed area was about 1 mm.

Thermal degradation of materials was evaluated by thermogravimetric analysis (TGA), which was carried out under N_2 flow (flow rate of 40 mL/min) using a TGAQ500-TA Instruments at a heating rate of 10 °C/min in the temperature range from 35 to 1000 °C.

Initial estimations of sheet resistance were made by using a multimeter to measure the resistance across 3 mm × 9 mm features. For CS/B40 and CS/B60 samples, two-terminal current−voltage measurements (±1 V, 20 mV step) were obtained under ambient conditions on transmission line method (TLM) structures using a Wentworth PML 8000 probe station and an Agilent E4980A parameter analyzer. Track resistance values for varying channel lengths were calculated from linear fits of I−V plots. Plots of track resistance versus channel length were used to calculate the sheet resistance (R_{SH}).

Electrochemical Measurements. Electrochemical measurements were recorded using a CHI760 bi-potentiostat. A three-

https://doi.org/10.1021/acssuschemeng.3c02708
ACS Sustainable Chem. Eng. 2023, 11, 13574−13583

electrode setup was used, with Ag/AgCl as the reference electrode and a Pt wire as the counter electrode. LIG was used as the working electrode. An electrode measuring 3 mm × 10 mm was scribed, and the surface was passivated using polyimide tape to reduce the active surface area to approximately 3 mm × 3 mm (see Figure 6a). The measurements were made in a Teflon electrochemical cell with the working electrode at the base. A 10 min electrochemical cleaning cycle was performed using 1 M KCl, in which the potential was varied between −1.6 and 0.8 V at a scan rate of 200 mV/s for 25 cycles. Afterward, 5 mM $[Fe(CN)_6]^{3-/4-}$ was used for standard electrode characterization. The calculation of the heterogeneous electron transfer (HET) rate constant (k^0) for $[Fe(CN)_6]^{3-/4-}$ was performed using the method of Nicholson by assuming a transfer coefficient α = 0.5 and using the following diffusion coefficients: $D_O = 7.63 \times 10^{-6}$ cm^2 s^{-1} and $D_R = 6.32 \times 10^{-6}$ $cm^2 s^{-1}$.[40]

RESULTS AND DISCUSSION

Figure 1 shows photographs of the CS/xB structures obtained at various laser power (LP) and laser speed (LS) values. The

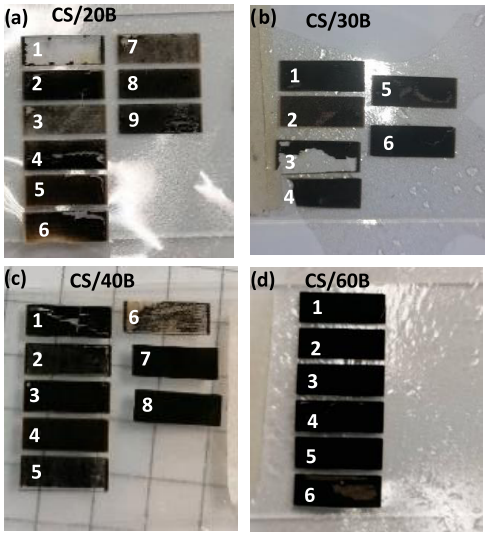

Figure 1. Effect of lasing of (a) CS/20B, (b) CS/30B, (c) CS/40B, and (d) CS/60B films by various laser parameters.

initial selection of optimal laser writing parameter optimization was determined by choosing the conditions that produced features with the highest conductivity (see Table S1). Figure 1 shows that the formation of LIG depended on the laser parameters as well as on the content of borax. In detail, Figure 1a shows that for CS/20B formulations, ablation and crack formation occurred for the majority of LP-LS combinations, preventing the formation of fully graphitized and low resistance features. Only one experimental writing condition (LP-LS 10−30 and two overlapped laser passes) led to the formation of LIG features, albeit with high $R_{sh} \geq 1$ kΩ/sq. An improvement in the graphitization process was observed in Figure 1b, where the borax content was increased to 30 wt %. As shown in Table S1, graphitized structures with R_{sh} of about 500 Ω/sq were formed using the combination LP-LS 10−20 and two overlapped laser passes. Figure 1c shows photographs of the features obtained by laser writing of CS/40B formulations, which had the required properties to allow graphitization with a range of laser settings (see details in Table S1), with low R_{sh} values reported for LP-LS 10−20 and two overlapped laser passes. Similarly, CS/60B formulations enabled LIG formation over a range of laser settings, as shown in Figure 1d. TLM measurements were performed on both LIG samples, as shown in Figure S1. The R_{sh} value for CS/40B-LIG was 110 ± 1, and that for CS/60B-LIG was 341 ± 6 Ω sq^{-1}. Overall, these results suggest that increasing the borax content improves the capacity of the material to withstand the high-temperature conditions necessary for the formation of LIG since graphitization of pure CS films with no borax content did not occur under any laser experimental conditions (see Figure S2).

CS/xB-LIG Characterization. To investigate the surface morphology, CS/xB-LIG features were examined by scanning electron microscopy (SEM). The SEM images shown in Figure 2a−h confirm that all samples displayed the porous, exploded structure associated with the LIG formation. This is a result of

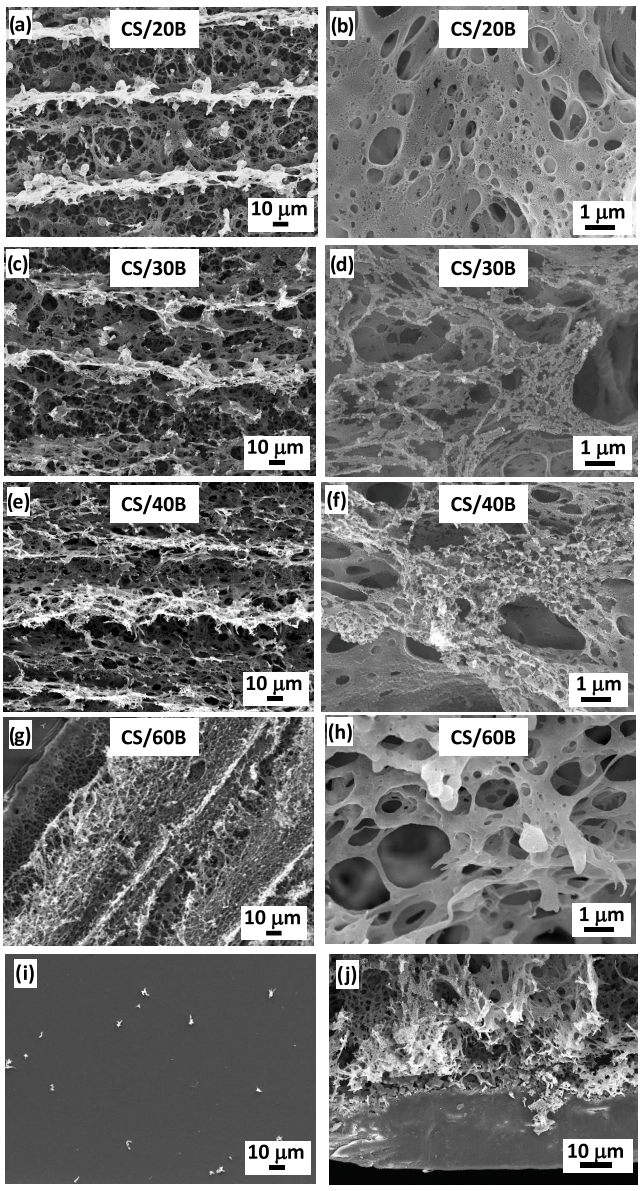

Figure 2. SEM images showing the process of laser graphitization on the CS/xB systems. Low-magnification SEM images of graphitized (a) CS/20B; (c) CS/30B; (e) CS/40B; and (g) CS/60B. High-magnification SEM images of (b) CS/20B; (d) CS/30B; (f) CS/40B; (h) CS/60B; (i) SEM image of pristine CS/40B; and (j) tilted SEM image of graphitized CS/40B.

https://doi.org/10.1021/acssuschemeng.3c02708
ACS Sustainable Chem. Eng. 2023, 11, 13574−13583

the laser impinging on the biopolymer substrate in the presence of atmospheric oxygen. Similar to what has been reported for laser writing of polyimide and other natural substrates, we speculate that the laser irradiation created a local high-temperature and high-pressure environment, leading to the breaking of the CS's C−O, C═O, and C−N bonds and to the formation of high-pressure gas pockets that drove the generation of micro and nanopores, along with other structural defects.[14,41−43] In general, high-magnification SEM images (Figure 2b,d,f,h) showed the formation of a dense and 3D graphitic network, with microholes and tears of different diameters on the LIG surface. Low-magnification images (Figure 2a,c,e,g) displayed the typical peaks and valleys associated with the raster scanning movement of the laser. For comparison, Figure 2i shows the SEM image of a pristine CS/40B film prior to graphitization, which was characterized by a smooth surface. Figure 2j shows a 45° angle tilted SEM image of a graphitized CS/40B sample, showing the LIG formation of about 35 μm thickness.

Figure 3 shows representative Raman spectra for LIG structures obtained from CS/xB formulations. For CS/20B,

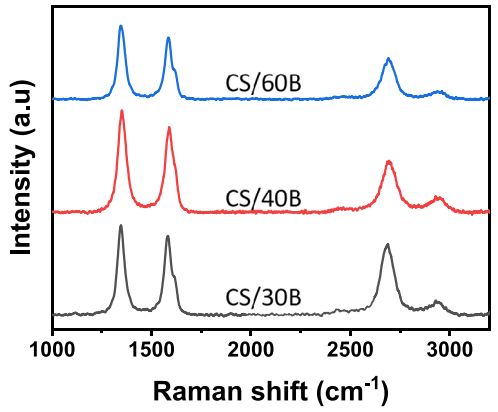

Figure 3. Representative Raman spectra of LIG structures obtained from direct laser writing of CS/xB biopolymer substrates.

Raman investigation confirmed the incomplete graphitization as spectra were either featureless or characterized by broad D, G, and two-dimensional (2D) peaks, highlighting an inhomogeneous distribution of graphene-like structures (see Figure S3).

For borax concentrations of 30 wt % and higher, each Raman spectrum showed well-resolved peaks, characteristic of graphene-like carbon structures: a D mode peak, assigned to a defect-activated radial breathing mode, centered close to 1350 cm^{-1}; a G mode peak, related to in-plane bond stretching of pairs of sp^2 carbon atoms, centered around 1584 cm^{-1}; and a 2D mode, the second order overtone of the D peak, centered around 2696 cm^{-1}.[44] A D′ peak was also fitted around 1618 cm^{-1}, evident in the asymmetry of the G peak, and associated with the formation of high-quality polycrystalline graphite or creation of defects in natural graphite single crystals.[45,46] A D + D′ appeared around 2940 cm^{-1} in the higher quality spectra. The formation of D and D + D′ bands is associated with the formation of graphene-like materials with significant defects originating from the intravalley double resonance and a combination mode, respectively.[47]

Peaks were fitted by a single Lorentzian curve. Twenty spectra were collected per LIG sample, with the average fitting results displayed in Table 1. The full width at half-maximum (FWHM) of both G, D, and 2D modes showed little variation

Table 1. Raman Characteristics of LIG Structures Obtained from Direct Laser Writing of CS/xB Formulation Substrates[a]

sample	$FWHM_D$ (cm^{-1})	$FWHM_G$ (cm^{-1})	$FWHM_{2D}$ (cm^{-1})	$I_{D/G}$	$I_{2D/G}$
CS/30B	41	38	69 ± 3	1.0 ± 0.1	0.8 ± 0.1
CS/40B	45 ± 1	39 ± 1	82 ± 2	1.2 ± 0.2	0.5 ± 0.1
CS/60B	49 ± 1	45 ± 1	84 ± 3	1.3 ± 0.1	0.5 ± 0.1

[a]Error reported is the standard deviation of 20 spectra. No error values were reported for standard deviation less than 0.5 cm^{-1}.

across samples (minimum for CS/30B), with all values remaining below 100 cm^{-1}. These sharp peaks suggest a high degree of crystallinity, and the FWHM values are in line with high-quality LIG produced on polyimide.[14] The I_D/I_G peak ratio was equal to 1 for CS/30B and only slightly increased for borax amounts ≥30 wt %, suggesting a low defect density. This result confirmed the nature of the LIG material, in agreement with the formation of highly ordered nanocrystalline graphitic domains in a disordered carbon matrix.[48] The relative intensity of the 2D peak also reached a maximum for the CS/30B formulation and then slowly decreased for higher boron concentrations. In parallel, the FWHM of the 2D peak reached a minimum for the CS/30B formulation and then slowly increased for higher boron content. The presence of sharp 2D peaks provided further evidence for a higher degree of ordering, consisting of randomly stacked graphene layers along the *c*-axis,[11] with the highest order observed for CS/30B and CS/40B structures. The high I_{2D}/I_G ratio indicated a low number of graphene layers.[11,48]

The CS/40B formulation was selected as optimal for further investigation and characterization, as it was easily graphitizable, and combined excellent Raman characteristics with the lowest sheet resistance (Figure S1).

CS/40B-LIG Characterization. Figure 4a shows a TEM image of a CS/40B-LIG structure displaying crystalline domains, better evidenced in the high-magnification inset, embedded in an amorphous matrix. The high-magnification TEM image (Figure 4a, inset) revealed the formation of multilayer structures, constituted by stacked graphene sheets, as well as nanoscale edges, ripples, and wrinkles, in agreement with the morphology of LIG samples obtained from other polymer and biopolymer matrices.[30] The calculated interlayer spacing was 3.5 Å (±0.1), which is similar to values determined for LIG on polyimide, wood, and cork.[11,15,24] Moreover, there is no morphological evidence of a separated borax phase, indicating that borax is incorporated and homogeneously distributed in the LIG structure. Further, TEM images are displayed in Figure S4, alongside details of interlayer spacing calculations.

Figure 4b shows the thermal stability of CS/40B films compared to the CS film, evaluated by TGA. The TGA curves presented different mass loss zones that were better highlighted in the corresponding DTA curves as shown in the inset of Figure 4b. The results show that the CS weight loss took place in two stages. The first one in the region of 60 to 160 °C, with a maximum temperature (Td_1) of 116 °C, was mainly ascribed to water evaporation. The second stage from 160 to 400 °C (two overlapping steps), with a maximum degradation

https://doi.org/10.1021/acssuschemeng.3c02708
ACS Sustainable Chem. Eng. 2023, 11, 13574−13583

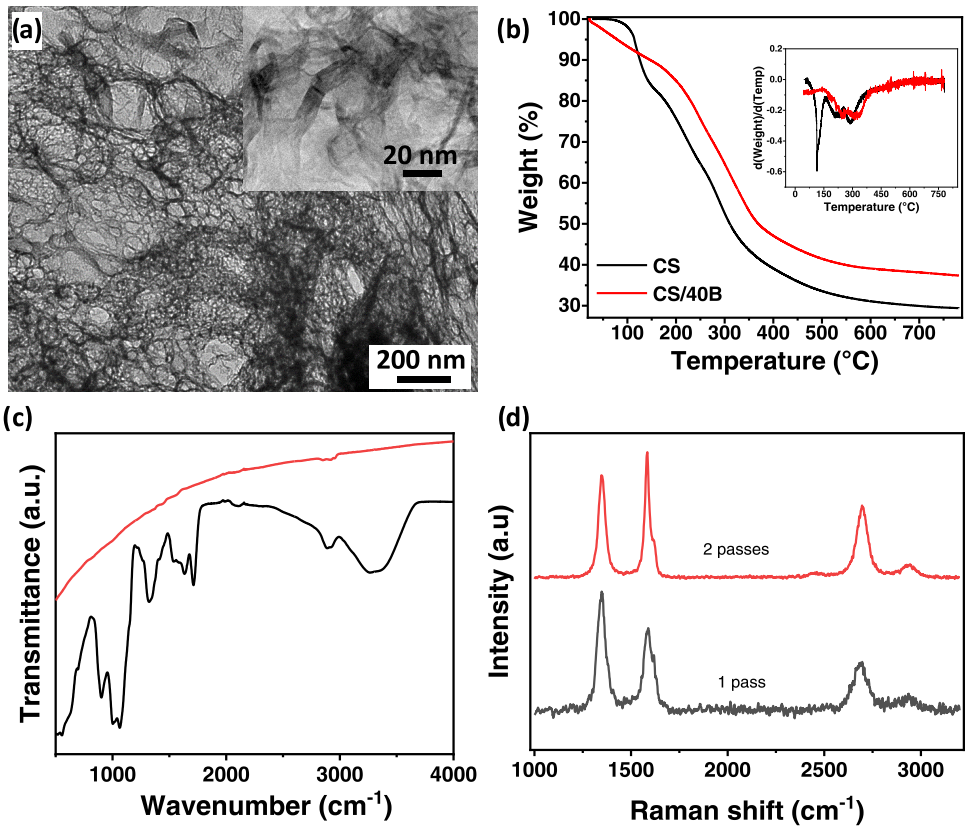

Figure 4. (a) TEM image of the LIG structure obtained from laser writing of CS/40B; (b) TGA of CS and CS/40B films. Inset: DTGA curves; (c) FTIR spectra of pristine CS/40B film (black line) and CS/40B-LIG structure (red line); and (d) Raman spectra after first and second laser pass.

temperature (Td_2) of 288°, was attributed to the pyrolysis of the polysaccharide that presumably started by a random split of the glycosidic bonds, followed by a further decomposition forming predominantly acetic, propionic, and butyric acids.[49] In the case of CS/40B films, the water loss occurred by a different mechanism compared to bare CS formulations due to the presence of borax, which can bind to water molecules, leading to stronger polymer−water interactions.[50] Moreover, due to the cross-linking between borax and the chitosan hydroxyl groups, the second stage of degradation showed a Td_2 value of 309 °C, which was 21 °C higher than the Td_2 of the bare CS sample. This temperature shift is probably due to a reduction of the concentration and availability of reactive OH groups in the CS/40B sample. At temperature lower than 400 °C, the anhydrous CS/40B sample converts to aliphatic char, which, in turn, at higher temperatures (≥400 °C) can give rise to cyclization, decarboxylation, decarbonylation, and cross-linking reactions, leading to the formation of aromatic char. It is also important to note that cross-linking of CS with borax increased the residual weight at 800 °C. A residual weight of 29 and 37% was found for CS and CS/40B films, respectively. These results highlight the ability of borax to promote the generation of char components.[32]

The process of LIG formation was analyzed further by spectroscopic characterization. Figure 4c shows ATR-FTIR spectra taken before and after graphitization. The as-fabricated chitosan film showed bands in good agreement with published work on chitosan films.[30,51−54] In the high wavenumber region of the spectrum (≥2600 cm^{-1}), common features were displayed: the band peaking at 3300 cm^{-1} caused by O−H stretching vibrations convoluted with N−H stretching and the band with a peak at 2890 cm^{-1} associated with C−H stretching vibrations. Such stretching vibrations are typical for polysaccharide molecules.[55] The presence of residual *N*-acetyl groups was confirmed by the presence of bands at 1636 cm^{-1} (C═C stretching of amide I) and 1535 cm^{-1} (N−H bending of amide II), respectively. The absorption peaks at 1064 and 896 cm^{-1} were ascribed to the antisymmetric stretching vibration of C−O−C bridges and glucopyranose ring in the chitosan matrix, suggesting an interaction between the glucopyranose ring in the chitosan matrix and borax.[56] In contrast, the FTIR spectrum of CS/40B-LIG was featureless, as expected for the conversion to graphitic and amorphous carbon.[15]

A more detailed analysis of the two-step graphitization process was performed by monitoring the change in Raman spectra between the first and second laser pass. The results are displayed in Figure 4d. The progression to a more ordered graphene-like material was clearly seen with the application of a second laser pass as the FWHM of all peaks decreased; the D peak intensity decreased while the G peak and 2D peak intensities increased. Moreover, the I_{2D}/I_G increased from 0.4 to 0.5, while the I_D/I_G ratio decreased from 1.5 to 1.2, indicating the progression to a higher degree of ordering in the sample.

Figure 5 shows the deconvoluted C 1s XPS spectra for the pristine CS/40B formulation and CS/40B-LIG. The graphitized sample was dominated by a large C 1s A peak, representing C═C sp^2 bonds. Other peaks have been labeled C 1s B (C−C), C (C−OH, −C−O), D (C═O), and E (carbonate). Peak assignments and percentage component concentrations are shown in Table 2. An increase in the

https://doi.org/10.1021/acssuschemeng.3c02708
ACS Sustainable Chem. Eng. 2023, 11, 13574−13583

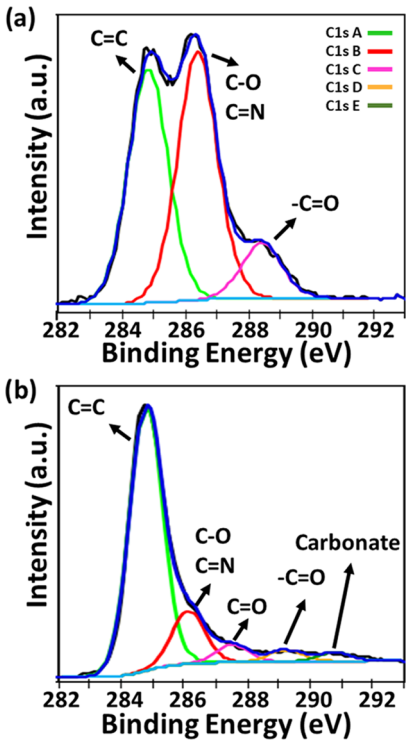

Figure 5. Deconvoluted XPS C 1S spectra of (a) pristine CS/40B film and (b) graphitized CS/40B.

Table 2. Summary of XPS Data for the CS/40B Pristine Sample and LIG Sample[a]

peak	atomic percentages (%) CS/40B	CS/40B-LIG	assignments
C 1s A	26.4	52.8	C−C sp^2
C 1s B	28.1	10.5	C−O, C−N
C 1s C	6.2	3.6	C═O
C 1s D		2.4	−C═O
C 1s E		1.8	carbonate
O 1s A	0.5		C−O
O 1s B	31	16.4	O═C
B 1s	2.4	7.5	$Na_2B_4O_7$ (a), B_2O_3 (b)
total C	60.7	71.1	
total O	31.5	16.4	
C 1s A/(B + C + D + E)	0.8	2.9	
C 1s A/O	0.8	3.2	

[a]For B 1s peak, (a) indicates peak assignment for CS/40B; (b) indicates assignment for CS/40B-LIG.

percentage of C═C carbon (graphene or graphite) was observed from 26.4% for untreated CS/40B to 52.8% for CS/40B-LIG. The concentration of sp^2 carbon doubled, and both the ratios of sp^2 carbon to other bonding forms and to oxygen content more than tripled. Also confirmed was the remaining surface carboxyl and carbonyl groups on the LIG sample, a useful surface feature for electrochemical applications. There was a substantial decrease in the total oxygen concentration in the CS/40B-LIG sample compared to the ungraphitized sample. In contrast, a relative increase in boron (from 2.4 to 7.5%) and sodium (from 3.2 to 4.6%) concentrations was observed in CS/40B-LIG samples compared to the ungraphitized samples (see Figure S5 and Table S3 for full range of XPS data). These data confirmed that borax facilitated the formation of LIG. Also, evidence of the formation of B_2O_3 as a result of the graphitization process was found from the XPS data. Overall, the XPS data confirmed that the CS/40B film was converted into LIG with a high sp^2 carbon content and the presence of surface oxygen groups and that B_2O_3 was embedded as an oxide in the LIG network.

Rationalizing the experimental results, it is possible to speculate that borax, thanks to its intrinsic ability to generate char[34] and in the case of polysaccharides to cross-link macromolecules,[32] is the key to allow the formation of graphitizable formulations. In fact, it is well known that borate ions can form covalent bonds with the hydroxyl moieties of CS by forming borate ester bonds, which contribute to densifying the polymeric network.[32,33] In the absence of B or at B percentage lower than 30 wt %, the direct laser writing of films resulted in CS degradation by polymer weight fragmentation and no formation of aromatic char. The formation of a cross-linked structure inhibits fragmentation of the polymer chain and likely improves char formation by cyclization and condensation.[36] The proposed graphitization mechanism is shown in Scheme 1.

A comprehensive overview of the characteristics of LIG derived from sustainable sources is provided in Table S2. The Raman characteristics (intensity ratios of D/G and 2D/G peaks) do not vary widely for LIG derived from sustainable precursors. The sheet resistances are generally reported between 10 and 125 Ω/sq, with some materials ranging to kΩ/sq. In this context, the work presented in this paper is more resistive than most reported. Importantly, in terms of application, this material property does not inhibit the performance of electrochemical devices in comparison with those made using chromatography paper, cork, or chitosan.

Electrochemical Characterization. An electrochemical characterization of CS/40B-LIG was performed to assess its capability as an electrode material for future electrochemical applications. Characterization was performed with a three-electrode electrochemical setup, whereby LIG was used as the working electrode. $[Fe(CN)_6]^{3-/4-}$, a standard redox probe, which undergoes a reversible one-electron reaction, was used for this investigation. Cyclic voltammetry (CV) was employed to investigate the electron transfer kinetics of the CS/40B-LIG electrode. Figure 6a shows the electrode design used, with the dotted line, indicating the area exposed to the analyte. The electrochemical cleaning of the electrode surface is shown in Figure 6b. The result of cycling in 1 M KCl for 10 min was the reduction of oxygen and oxygenated groups at −0.4 and −1.2 V, respectively.[57]

The effect of this electrochemical cleaning is seen in the inset of Figure 6b. The oxidation and reduction peak currents of $[Fe(CN)_6]^{3-/4-}$ increased in magnitude, the peaks became sharper, and a reduced peak separation was observed. Figure 6c shows the cyclic voltammetry curves of $Fe(CN)_6^{3-/4-}$ measured between 10 and 100 mV/s scan rates. Fast electron transfer rates were observed, with ΔE_p values below 80 mV at 10 mV/s and below 200 mV up to scan rates of 500 mV/s. The inset of Figure 6c shows the linear plots of peak current (oxidation current and reduction current) with the square root of the scan rate, in line with the Randles−Ševčík equation and indicating a semi-infinite linear diffusion regime. Monitoring the values of ΔE_p with changing scan rate allowed for the determination of the hetero electron transfer rate (k^0) by the Nicholas method. The value calculated for this material was 4 × 10^{-3} cm s^{-1}. A comparison with literature values for

https://doi.org/10.1021/acssuschemeng.3c02708
ACS Sustainable Chem. Eng. 2023, 11, 13574−13583

Scheme 1. Proposed Mechanism of Action of Borax in LIG Formation

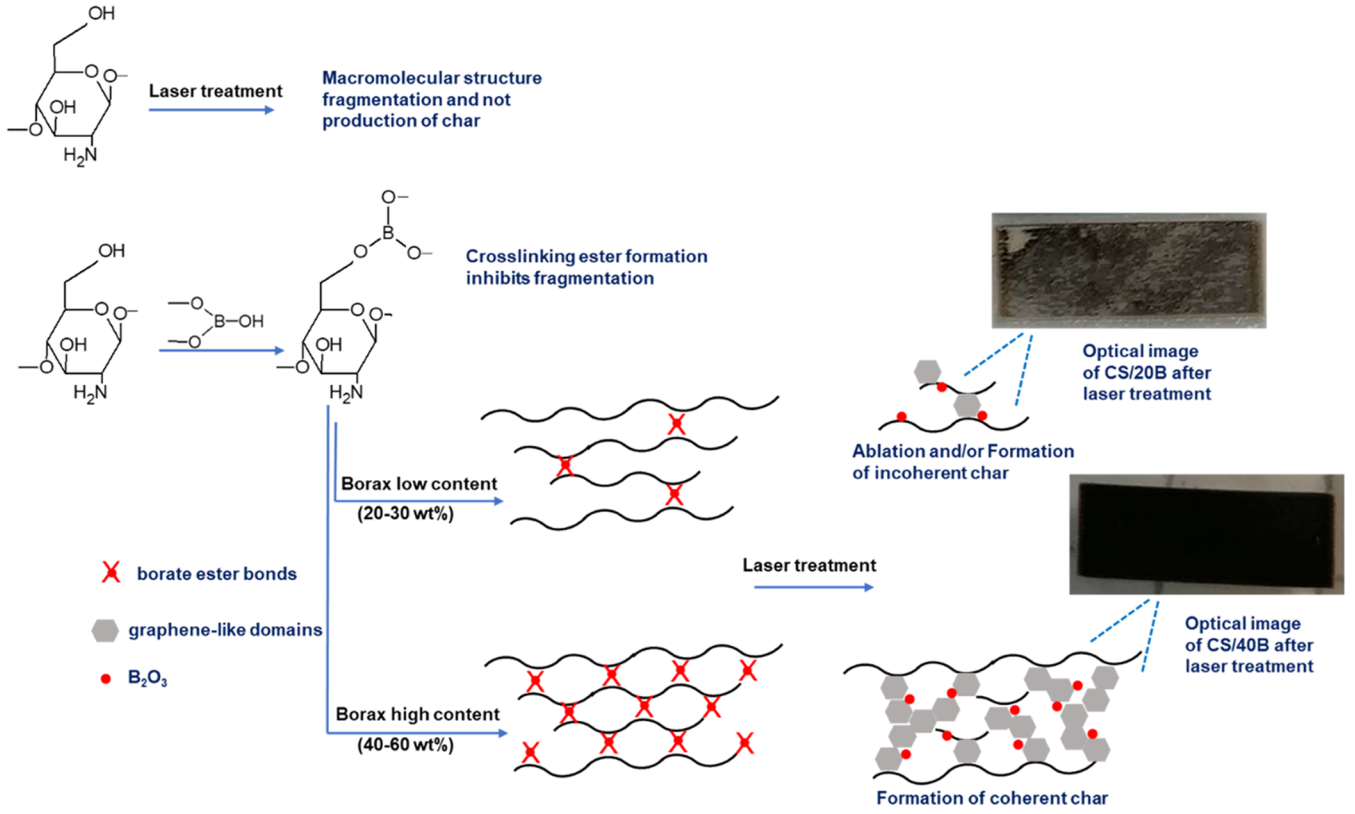

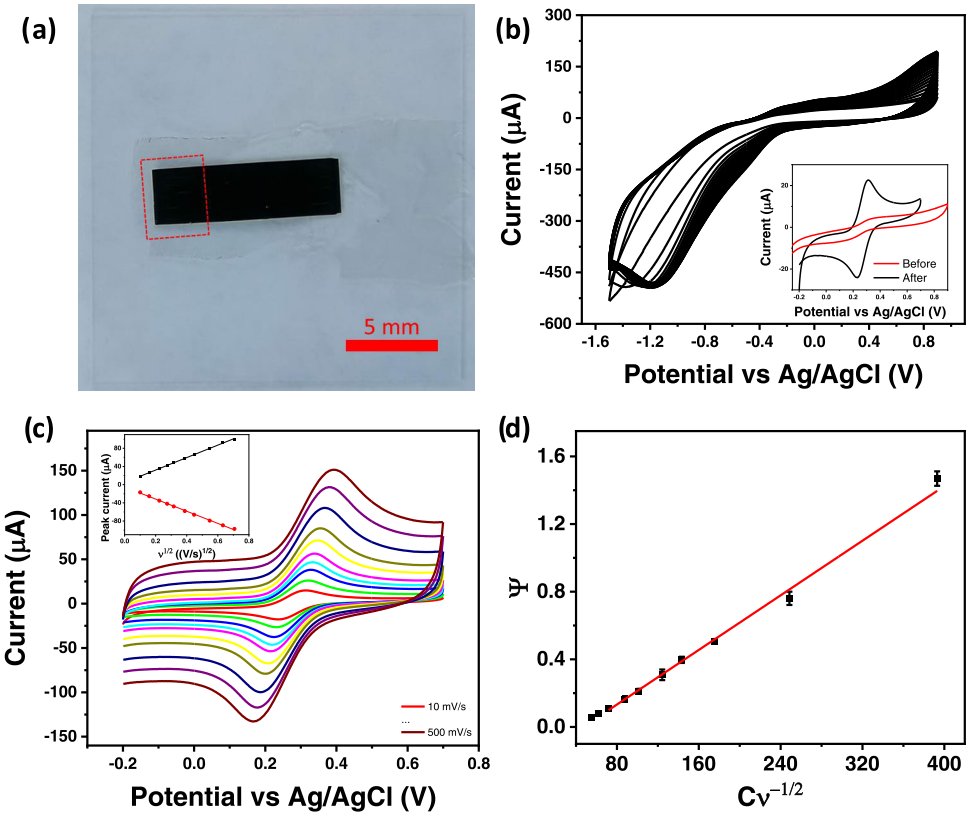

Figure 6. (a) LIG electrode design with exposed area outlined by a dotted red square; (b) cleaning cycles in 1 M KCl with oxygen reduction beginning around −0.5 V and oxygenated group reduction peak appearing around −1.2 V. Inset showing the effect of cleaning cycles on sensing of $Fe(CN)_6^{3-/4-}$; (c) cyclic voltammetry (CV) scans at varying scan rates for 5 mM $Fe(CN)_6^{3-/4-}$ in 1 M KCl. Inset shows peak oxidation and reduction current with the square root of scan rate; (d) k^0 calculation by the Nicholson method.

https://doi.org/10.1021/acssuschemeng.3c02708
ACS Sustainable Chem. Eng. 2023, 11, 13574−13583

$[Fe(CN)_6]^{3-/4}$, including LIG on polyimide as a benchmark, is provided in Table 3. The k^0 value presented in this work is an order of magnitude larger than values seen for LIG on paper substrates and much improved from electrochemical results previously reported for LIG on a chitosan-based biofilm. In 59, the electrochemical sensor was water-soluble, leading to a breakdown with time. The improvement of the water barrier properties of the chitosan−borax films presented in this paper allows for more stable devices. The rapid electron transfer kinetics presented here mean that this material is suitable for further use as an electrochemical sensing platform.

Table 3. Comparison of Electron Transfer Properties for Ferrocyanide with Literature Values for LIG on Polyimide and Natural Precursors[a]

material	laser	ΔE_p (mV)	$k_{app}{}^0$ (cm s^{-1})	refs
polyimide	450 nm	61	1.26×10^{-1}	14
polyimide	405 nm	86	1.3×10^{-2}	48
filter paper	10.6 μm		7.8×10^{-4}	58
office paper	10.6 μm	≥700	4.08×10^{-4}	39
chromatography paper	10.6 μm	370	6.85×10^{-4}	39
chitosan	10.6 and 405 nm	290		59
cork	450 nm	90	9×10^{-3}	60
chitosan−borax	10.6 μm	110	4×10^{-3}	this work

[a] ΔE_p for ν between 50−150 mV s^{-1} (100 mV s^{-1} for this work).

These results present an advanced material from renewable sources. Green LIG sensors are suitable for a variety of Internet of Things applications. The surface qualities of LIG allow for facile modification of the surface, making this an ideal platform for a green-biosensing platform.

CONCLUSIONS

The successful conversion of CS/xB formulations into high-quality LIG has been presented. It was found that 40% wt. borax (with respect to CS weight) was the optimal content by monitoring the electrical and Raman parameters of LIG. Borax content in the formulations' composition was found to play an important role in the formation of LIG by acting as a cross-linking agent for chitosan and due to its flame-retardant properties, which facilitated the high-temperature conditions necessary for LIG formation. The derived CS/40B-LIG displayed excellent properties as an electrochemical sensing platform. The k^0 value determined for $[Fe(CN)_6]$, 4×10^{-3} cm s^{-1} is higher than that calculated for most other green LIG sensors and is higher than previous works on chitosan-based LIG. This showcases the potential for this material in future electrochemical applications. These CS-based films offer an important, environmentally friendly route to creating LIG materials, an alternative to fossil fuel-derived synthetic polymers.

ASSOCIATED CONTENT

Data Availability Statement

The data presented in this article are available from the author upon reasonable request.

Supporting Information

The Supporting Information is available free of charge at https://pubs.acs.org/doi/10.1021/acssuschemeng.3c02708.

Additional electrical data for optimizing laser parameters; chitosan sheet in the absence of borax; Raman spectroscopy of CS/20B; table of comparison with literature for LIG from natural precursors; additional TEM images and lattice spacing calculations; XPS O 1s, B 1s and Na 1s spectra for CS/40B-LIG; HET rate calculations (PDF)

AUTHOR INFORMATION

Corresponding Authors

Eoghan Vaughan − *Tyndall National Institute, University College Cork, Cork T12R5CP, Ireland;* orcid.org/0000-0002-9524-0204; Email: eoghan.vaughan@tyndall.ie

Marino Lavorgna − *Institute for Polymers, Composites and Biomaterials, National Research Council of Italy, 80055 Portici, Italy;* orcid.org/0000-0002-4705-4378; Email: mlavorgna@unina.it

Daniela Iacopino − *Tyndall National Institute, University College Cork, Cork T12R5CP, Ireland;* orcid.org/0000-0003-2301-9401; Email: daniela.iacopino@tyndall.ie

Authors

Chiara Santillo − *Institute for Polymers, Composites and Biomaterials, National Research Council of Italy, 80055 Portici, Italy*

Alessandra Imbrogno − *Tyndall National Institute, University College Cork, Cork T12R5CP, Ireland*

Gennaro Gentile − *Institute for Polymers Composites and Biomaterials, National Research Council of Italy, 80078 Pozzuoli, Italy;* orcid.org/0000-0002-1280-8926

Aidan J. Quinn − *Tyndall National Institute, University College Cork, Cork T12R5CP, Ireland;* orcid.org/0000-0003-4021-9990

Saulius Kaciulis − *Institute for the Study of Nanostructured Materials, National Research Council, 00015 Rome, Italy*

Complete contact information is available at: https://pubs.acs.org/10.1021/acssuschemeng.3c02708

Author Contributions

[⊥]E.V. and C.S. contributed equally to this work. This manuscript was written through contributions of all authors. All authors have given approval to the final version of the manuscript.

Funding

This publication has emanated from research conducted with the financial support of the European Union H2021 project Greenart (101060941) project; Science Foundation Ireland (SFI) under the European Regional Development Fund Grant Number 13/RC/2077-P2 (CONNECT) and 16/RC/3918 (CONFIRM); and Science Foundation Ireland (SFI) and the Department of Agriculture, Food, and Marine on behalf of the Government of Ireland under Grant Number 16/RC/3835 (VISTAMILK).

Notes

The authors declare no competing financial interest.

ACKNOWLEDGMENTS

The authors acknowledge Alessandra Aldi (IPCB-CNR) and Mario De Angioletti (IPCB-CNR) for the technical assistance in the experiments.

REFERENCES

(1) Novoselov, K. S.; Geim, A. K.; Morozov, S. V.; Jiang, D.; Zhang, Y.; Dubonos, S. V.; Grigorieva, I. V.; Firsov, A. A. Electric Field Effect in Atomically Thin Carbon Films. *Science* **2004**, *306*, 666−669.

(2) Zhu, J.; Yang, D.; Yin, Z.; Yan, Q.; Zhang, H. Graphene and Graphene-Based Materials for Energy Storage Applications. *Small* **2014**, *10*, 3480−3498.

(3) Nag, A.; Mitra, A.; Mukhopadhyay, S. C. Graphene and its sensor-based applications: A review. *Sens. Actuators, A* **2018**, *270*, 177−194.

(4) Olabi, A. G.; A, M. A.; Wilberforce, T.; Sayed, E. T. Application of graphene in energy storage device − A review. *Renewable Sustainable Energy Rev.* **2021**, *135*, No. 110026.

(5) Bae, S.-H.; L, Y.; Sharma, B. K.; Lee, H.-J.; Kim, J.-H.; Ahn, J.-H. Graphene-based transparent strain sensor. *Carbon* **2013**, *51*, 236−242.

(6) Yam, K. M.; Guo, N.; Jiang, Z.; Li, S.; Zhang, C. Graphene-Based Heterogeneous Catalysis: Role of Graphene. *Catalysts* **2020**, *10*, No. 53.

(7) Ramesh, R. Graphene: Fabrication Methods, Properties, and Applications in Modern Industries. In *Graphene Production and Application*; Sadia, A.; Akhtar, M. S.; Hyung-Shik, S., Eds.; IntechOpen: Rijeka, 2020.

(8) Cote, L. J.; Cruz-Silva, R.; Huang, J. Flash Reduction and Patterning of Graphite Oxide and Its Polymer Composite. *J. Am. Chem. Soc.* **2009**, *131*, 11027−11032.

(9) Mukherjee, R.; Thomas, A. V.; Krishnamurthy, A.; Koratkar, N. Photothermally Reduced Graphene as High-Power Anodes for Lithium-Ion Batteries. *ACS Nano* **2012**, *6*, 7867−7878.

(10) El-Kady, M. F.; Strong, V.; Dubin, S.; Kaner, R. B. Laser Scribing of High-Performance and Flexible Graphene-Based Electrochemical Capacitors. *Science* **2012**, *335*, 1326−1330.

(11) Lin, J.; Peng, Z.; Liu, Y.; Ruiz-Zepeda, F.; Ye, R.; Samuel, E. L. G.; Yacaman, M. J.; Yakobson, B. I.; Tour, J. M. Laser-induced porous graphene films from commercial polymers. *Nat. Commun.* **2014**, *5*, No. 5714.

(12) Vivaldi, F. M.; Dallinger, A.; Bonini, A.; Poma, N.; Sembranti, L.; Biagini, D.; Salvo, P.; Greco, F.; Di Francesco, F. Three-Dimensional (3D) Laser-Induced Graphene: Structure, Properties, and Application to Chemical Sensing. *ACS App. Mater. Interfaces* **2021**, *13*, 30245−30260.

(13) Wang, L.; Wang, Z.; Bakhtiyari, A. N.; Bakhtiyari, A. N.; Zheng, H. A Comparative Study of Laser-Induced Graphene by CO2 Infrared Laser and 355 nm Ultraviolet (UV) Laser. *Micromachines* **2020**, *11*, No. 1094.

(14) Vaughan, E.; Larrigy, C.; Burke, M.; Sygellou, L.; Quinn, A. J.; Galiotis, C.; Iacopino, D. Visible Laser Scribing Fabrication of Porous Graphitic Carbon Electrodes: Morphologies, Electrochemical Properties, and Applications as Disposable Sensor Platforms. *ACS App. Electron. Mater.* **2020**, *2*, 3279−3288.

(15) Imbrogno, A.; Islam, J.; Santillo, C.; Castaldo, R.; Sygellou, L.; Larrigy, C.; Murray, R.; Vaughan, E.; Hoque, M. K.; Quinn, A. J.; Iacopino, D. Laser-Induced Graphene Supercapacitors by Direct Laser Writing of Cork Natural Substrates. *ACS Appl. Electron. Mater.* **2022**, *4*, 1541−1551.

(16) Tan, P. S.; Vaughan, E.; Islam, J.; Burke, N.; Iacopino, D.; Tierney, J. B. Laser Scribing Fabrication of Graphitic Carbon Biosensors for Label-Free Detection of Interleukin-6. *Nanomaterials* **2021**, *11*, No. 2110.

(17) Madden, J.; Vaughan, E.; Thompson, M.; Riordan, A. O.; Galvin, P.; Iacopino, D.; Teixeira, S. R. Electrochemical sensor for enzymatic lactate detection based on laser-scribed graphitic carbon modified with platinum, chitosan and lactate oxidase. *Talanta* **2022**, *246*, No. 123492.

(18) Paterakis, G.; Vaughan, E.; Gawade, D. R.; Murray, R.; Gorgolis, G.; Matsalis, S.; Anagnostopoulos, G.; Buckley, J. L.; O'Flynn, B.; Quinn, A. J.; Iacopino, D.; Galiotis, C. Highly Sensitive and Ultra-Responsive Humidity Sensors Based on Graphene Oxide Active Layers and High Surface Area Laser-Induced Graphene Electrodes. *Nanomaterials* **2022**, *12*, No. 2684.

(19) Liu, J.; Ji, H.; Lv, X.; Zeng, C.; Li, H.; Li, F.; Qu, B.; Cui, F.; Zhou, Q. Laser-induced graphene (LIG)-driven medical sensors for health monitoring and diseases diagnosis. *Microchim. Acta* **2022**, *189*, No. 54.

(20) Yang, Y.; Song, Y.; Bo, X.; Min, J.; Pak, O. S.; Zhu, L.; Wang, M.; Tu, J.; Kogan, A.; Zhang, H.; Hsiai, T. K.; Li, Z.; Gao, W. A laser-engraved wearable sensor for sensitive detection of uric acid and tyrosine in sweat. *Nat. Biotechnol.* **2020**, *38*, 217−224.

(21) Pirson, T.; Bol, D. Assessing the embodied carbon footprint of IoT edge devices with a bottom-up life-cycle approach. *J. Cleaner Prod.* **2021**, *322*, No. 128966.

(22) Piro, B.; Tran, H. V.; Thu, V. T. Sensors Made of Natural Renewable Materials: Efficiency, Recyclability or Biodegradability-The Green Electronics. *Sensors* **2020**, *20*, No. 5898.

(23) Vashisth, A.; Kowalik, M.; Gerringer, J. C.; Ashraf, C.; van Duin, A. C. T.; Green, M. J. ReaxFF Simulations of Laser-Induced Graphene (LIG) Formation for Multifunctional Polymer Nanocomposites. *ACS Appl. Nano Mater.* **2020**, *3*, 1881−1890.

(24) Ye, R.; Chyan, Y.; Zhang, J.; Li, Y.; Han, X.; Kittrell, C.; Tour, J. M. Laser-Induced Graphene Formation on Wood. *Adv. Mater.* **2017**, *29*, No. 1702211.

(25) de Araujo, W. R.; Frasson, C. M. R.; Ameku, W. A.; Silva, J. R.; Angnes, L.; Paixão, T. R. L. C. Single-Step Reagentless Laser Scribing Fabrication of Electrochemical Paper-Based Analytical Devices. *Angew. Chem., Int. Ed.* **2017**, *56*, 15113−15117.

(26) Le, T. D.; Park, S.; An, J.; Lee, P. S.; Kim, Y.-J. Ultrafast Laser Pulses Enable One-Step Graphene Patterning on Woods and Leaves for Green Electronics. *Adv. Funct. Mater.* **2019**, *29*, No. 1902771.

(27) Zhang, C.; Xie, Y.; Zhang, C.; Lin, J. Upgrading coal to multifunctional graphene-based materials by direct laser scribing. *Carbon* **2019**, *153*, 585−591.

(28) Chyan, Y.; Ye, R.; Li, Y.; Singh, S. P.; Arnusch, C. J.; Tour, J. M. Laser-Induced Graphene by Multiple Lasing: Toward Electronics on Cloth, Paper, and Food. *ACS Nano* **2018**, *12*, 2176−2183.

(29) Claro, P. I.; Pinheiro, T.; Silvestre, S. L.; Marques, A. C.; Coelho, J.; Marconcini, J. M.; Fortunato, E.; C Mattoso, L. H.; Martins, R. Sustainable carbon sources for green laser-induced graphene: A perspective on fundamental principles, applications, and challenges. *Appl. Phys. Rev.* **2022**, *9*, No. 041305.

(30) Larrigy, C.; Burke, M.; Imbrogno, A.; Vaughan, E.; Santillo, C.; Lavorgna, M.; Sygellou, L.; Paterakis, G.; Galiotis, C.; Iacopino, D.; Quinn, A. J. Porous 3D Graphene from Sustainable Materials: Laser Graphitization of Chitosan. *Adv. Mat. Technol.* **2022**, *8*, No. 2201228.

(31) Huang, Q.-M.; Yang, H.; Wang, S.; Liu, X.; Tan, C.; Luo, A.; Xu, S.; Zhang, G.; Ye, H. Laser-Induced Graphene Formation on Chitosan Derivatives toward Ecofriendly Electronics. *ACS Appl. Nano Mater.* **2023**, *6*, 10453−10465.

(32) Santillo, C.; Wang, Y.; Buonocore, G. G.; Gentile, G.; Verdolotti, L.; Kaciulis, S.; Xia, H.; Lavorgna, M. Hybrid Graphenene Oxide/Cellulose Nanofillers to Enhance Mechanical and Barrier Properties of Chitosan-Based Composites. *Front. Chem.* **2022**, *10*, No. 926364.

(33) Yan, N.; Capezzuto, F.; Lavorgna, M.; Buonocore, G. G.; Tescione, F.; Xia, H.; Ambrosio, L. Borate cross-linked graphene oxide−chitosan as robust and high gas barrier films. *Nanoscale* **2016**, *8*, 10783−10791.

(34) Dogan, M.; Dogan, S. D.; Savas, L. A.; Ozcelik, G.; Tayfun, U. Flame retardant effect of boron compounds in polymeric materials. *Composites, Part B* **2021**, *222*, No. 109088.

(35) Wang, F.; Liu, J.; Lv, W. Thermal degradation and fire performance of wood treated with PMUF resin and boron compounds. *Fire Mater.* **2017**, *41*, 1051−1057.

(36) Wicklein, B.; Kocjan, D.; Carosio, F.; Camino, G.; Bergström, L. Tuning the Nanocellulose−Borate Interaction To Achieve Highly Flame Retardant Hybrid Materials. *Chem. Mater.* **2016**, *28*, 1985−1989.

https://doi.org/10.1021/acssuschemeng.3c02708
ACS Sustainable Chem. Eng. 2023, 11, 13574−13583

(37) Duquesne, S.; Bourbigot, S.Char Formation and Characterization. In *Fire Retardancy Polym. Mater.*, 2nd ed.; CRC, 2009; pp 239−259.
(38) Coelho, J.; Correia, R. F.; Silvestre, S.; Pinheiro, T.; Marques, A. C.; Correia, M. R. P.; Pinto, J. V.; Fortunato, E.; Martins, R. Paper-based laser-induced graphene for sustainable and flexible micro-supercapacitor applications. *Microchim. Acta* **2023**, *190*, No. 40.
(39) Pinheiro, T.; Silvestre, S.; Coelho, J.; Marques, A. C.; Martins, R.; Sales, M. G. F.; Fortunato, E. Laser-Induced Graphene on Paper toward Efficient Fabrication of Flexible, Planar Electrodes for Electrochemical Sensing. *Adv. Mater Interfaces* **2021**, *8*, No. 2101502.
(40) Konopka, S. J.; McDuffie, B. Diffusion coefficients of ferri- and ferrocyanide ions in aqueous media, using twin-electrode thin-layer electrochemistry. *Anal. Chem.* **1970**, *42*, 1741−1746.
(41) Dreyfus, R. W. CN temperatures above laser ablated polyimide. *Appl. Phys. A: Solids Surf.* **1992**, *55*, 335−339.
(42) Ye, R.; James, D. K.; Tour, J. M. Laser-Induced Graphene: From Discovery to Translation. *Adv. Mater.* **2019**, *31*, No. 1803621.
(43) Dong, Y.; Rismiller, S. C.; Lin, J. Molecular dynamic simulation of layered graphene clusters formation from polyimides under extreme conditions. *Carbon* **2016**, *104*, 47−55.
(44) Childres, I.; Jauregui, L. A.; Park, W.; Cao, H.; Chen, Y. P. Raman spectroscopy of graphene and related materials. *New Dev. Photon Mater. Res.* **2013**, *1*, 1−20.
(45) Lespade, P.; Al-Jishi, R.; Dresselhaus, M. S. Model for Raman scattering from incompletely graphitized carbons. *Carbon* **1982**, *20*, 427−431.
(46) Nemanich, R. J.; Glass, J. T.; Lucovsky, G.; Shroder, R. E. Raman scattering characterization of carbon bonding in diamond and diamondlike thin films. *J. Vac. Sci. Technol., A* **1988**, *6*, 1783−1787.
(47) Hong, J.; Park, M. K.; Lee, E. J.; Lee, D.; Hwang, D. S.; Ryu, S. Origin of New Broad Raman D and G Peaks in Annealed Graphene. *Sci. Rep.* **2013**, *3*, No. 2700.
(48) Burke, M.; Larrigy, C.; Vaughan, E.; Paterakis, G.; Sygellou, L.; Quinn, A. J.; Herzog, G.; Galiotis, C.; Iacopino, D. Fabrication and Electrochemical Properties of Three-Dimensional (3D) Porous Graphitic and Graphenelike Electrodes Obtained by Low-Cost Direct Laser Writing Methods. *ACS Omega* **2020**, *5*, 1540−1548.
(49) Neto, C. G. T.; Giacometti, J. A.; Job, A. E.; Ferreira, F. C.; Fonseca, J. L. C.; Pereira, M. R. Thermal Analysis of Chitosan Based Networks. *Carbohydr. Polym.* **2005**, *62*, 97−103.
(50) Santillo, C.; Wang, Y.; Buonocore, G. G.; Gentile, G.; Verdolotti, L.; Kaciulis, S.; Xia, H.; Lavorgna, M. Hybrid Graphenene Oxide/Cellulose Nanofillers to Enhance Mechanical and Barrier Properties of Chitosan-Based Composites. *Front. Chem.* **2022**, *10*, No. 926364.
(51) Grossutti, M.; Dutcher, J. R. Correlation Between Chain Architecture and Hydration Water Structure in Polysaccharides. *Biomacromolecules* **2016**, *17*, 1198−1204.
(52) Lawrie, G.; Keen, I.; Drew, B.; Chandler-Temple, A.; Rintoul, L.; Fredericks, P.; Grøndahl, L. Interactions between Alginate and Chitosan Biopolymers Characterized Using FTIR and XPS. *Biomacromolecules* **2007**, *8*, 2533−2541.
(53) Ritthidej, G. C.; Phaechamud, T.; Koizumi, T. Moist heat treatment on physicochemical change of chitosan salt films. *Int. J. Pharm.* **2002**, *232*, 11−22.
(54) Qiao, C.; Ma, X.; Zhang, J.; Yao, J. Molecular interactions in gelatin/chitosan composite films. *Food Chem.* **2017**, *235*, 45−50.
(55) Yusof, N. H.; Foo, K. Y.; Wilson, L. D.; Hameed, B. H.; Hussin, M. H.; Sabar, S. Microwave-Assisted Synthesis of Polyethyleneimine Grafted Chitosan Beads for the Adsorption of Acid Red 27. *J. Polym. Environ.* **2020**, *28*, 542−552.
(56) Shankar, S.; Rhim, J.-W. Bionanocomposite Films for Food Packaging Applications. In *Reference Module in Food Science*; Elsevier, 2018.
(57) Vivaldi, F.; Dallinger, A.; Poma, N.; Bonini, A.; Biagini, D.; Salvo, P.; Borghi, F.; Tavanti, A.; Greco, F.; Di Francesco, F. Sweat analysis with a wearable sensing platform based on laser-induced graphene. *APL Bioeng.* **2022**, *6*, No. 036104.
(58) Kulyk, B.; Pereira, S. O.; Fernandes, A. J. S.; Fortunato, E.; Costa, F. M.; Santos, N. F. Laser-induced graphene from paper for non-enzymatic uric acid electrochemical sensing in urine. *Carbon* **2022**, *197*, 253−263.
(59) Larrigy, C.; Burke, M.; Imbrogno, A.; Vaughan, E.; Santillo, C.; Lavorgna, M.; Sygellou, L.; Paterakis, G.; Galiotis, C.; Iacopino, D.; Quinn, A. J. Porous 3D Graphene from Sustainable Materials: Laser Graphitization of Chitosan. *Adv. Mater. Technol.* **2023**, *8*, No. 2201228.
(60) Vaughan, E.; Santillo, C.; Setti, M.; Larrigy, C.; Quinn, A. J.; Gentile, G.; Lavorgna, M.; Iacopino, D. Sustainable Laser-Induced Graphene Electrochemical Sensors from Natural Cork for Sensitive Tyrosine Detection. *Adv. Sens. Res.* **2023**, No. 2300026.

https://doi.org/10.1021/acssuschemeng.3c02708
ACS Sustainable Chem. Eng. 2023, 11, 13574−13583